Ice and gas in protostellar clouds and planet-forming disks: a combined laboratory and observational study

Terwisscha van Scheltinga, J.

Citation

Terwisscha van Scheltinga, J. (2021, November 30). *Ice and gas in protostellar clouds and planet-forming disks: a combined laboratory and observational study*. Retrieved from https://hdl.handle.net/1887/3245869

2 | METHODS

The data presented in this thesis is either measured in the Laboratory for Astrophysics at Leiden Observatory or with the Atacama Large millimiter/submillimeter Array (ALMA). This chapter is for the reader who is less familiar with laboratory astrophysics and radio interferometry in general and acts as a bridge between Chapter 1 and the subsequent research chapters. It adds detail to the rather concise information presented in Chapters 3, 4, 5, and 6, focusing on general procedures and calibrations.

2.1 HV setup

The HV setup is used to measure the infrared spectra of COMs in pure form and mixed with astronomically relevant ice matrices in Chapters 3 and 4. At the heart of this setup is a stainless steel chamber, which is positioned in the sample compartment of a Varian 670 Fourier transform infrared (FTIR) spectrometer, see Figure 2.1. The chamber is pumped by a 350 l s^{-1} turbomolecular pump (Oerlikon Leybold TurboVac 361), which is backed by a double-stage rotary vane pump (8 m^3 h^{-1}, Edwards E2M8). This allows for a base pressure of $\sim 2 \times 10^{-7}$ mbar at room temperature, and is monitored with a Agilent FRG-720 full range gauge. The center of the vacuum chamber houses a ZnSe window that is cooled down to a temperature of 12 K by a closed-cycle helium refrigerator (Air Products Displex DE-202). The temperature of the ZnSe window is measured by a temperature sensor (silicon diode DT-670-CU), which is connected to a LakeShore 330 temperature controller. This PID controller actively controls the temperature by measuring the difference between the measured and desired temperature. If there is a difference, the PID controller changes the Joule heating of the ZnSe window to reach the desired temperature. ZnSe is largely transparent for infrared light, and allows for transmission vibrational spectroscopy of species deposited on the window. The FTIR spectrometer records spectra at a resolution as accurate as 0.1 cm^{-1} in the 4000–400 cm^{-1} (2.5–25 μm) range. The optical path of the infrared light is purged with dry air to prevent absorption by CO_2 and H_2O in the atmosphere (Balston 75-62 FT-IR Purge Gas Generator). The deposition of species on the ZnSe window occurs through careful admission of gas-phase samples with a needle valve.

The samples of gas or vapor are stored in a 2 liter glass bulb, which is connected to the deposition line of the HV setup. The glass bulb is filled on a different setup, namely our mixing line, see Figure 2.2. This mixing line has its own pre-vacuum pump and turbomolecular pump and allows pumping down to pressures $< 10^{-5}$ mbar to ensure there is no contamination of atmosphere or previously used gasses or vapors.

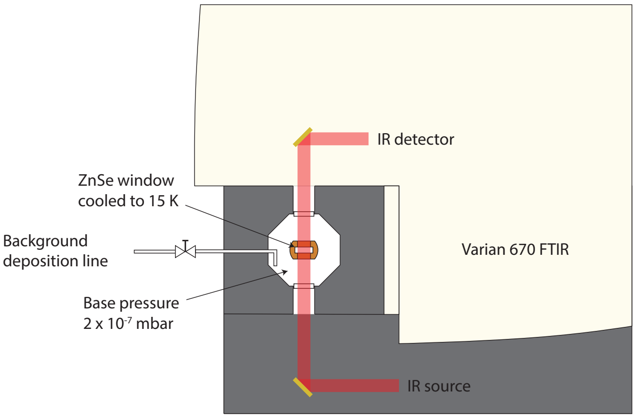

Figure 2.1: Schematic drawing of the HV setup. A simplified pathway of the infrared is shown in red. The ZnSe window is mounted at the bottom of the second stage of the closed-cycle helium refrigerator.

The mixing line features two gas-independent pressure gauges (Edwards 600AB Trans 10MB and 1000MB) that measure in the range of 0–10 and 0–1000 mbar. In general, glass bulbs are filled with 20 mbar of a pure or mixed gasses and vapors. This pressure is not arbitrarily chosen as it ensures that H_2O does not condense on the glass surface. This is because the vapor pressure of H_2O at room temperature is approximately 23 mbar. By careful measuring the exact volume of the mixing line and the glass bulb, the ideal gas law can be used to make accurate mixtures. Additionally, the bottom of the glass bulb can be placed in a liquid nitrogen (LN_2) bath, which allows molecules such as water, methanol, or any COM to freeze out at the bottom of the glass bulb. An advantage of this is that as long as the bulb is in placed in LN_2 bath, other mixture components can be added sequentially as long as their freeze-out temperature is above the temperature of LN_2, approximately 77 K. For example, assuming that the ratio between the glass bulb and mixing line is 10. A mixture with a total pressure of 20 mbar of CO, methanol, and ethanol in a ratio of 10:10:1 (9.5:9.5:0.95 mbar) is realized as follows:

1. Connect glass bulb to mixing line and evacuate both to a pressure of at least $< 10^{-5}$ mbar.
2. Close valve between the glass bulb and mixing line, henceforth valve, and place a LN_2 bath around the bottom of the glass bulb.
3. Fill the mixing line with 9.5 (10×0.95) mbar of ethanol and open the valve. The ethanol freezes out at the bottom, and given that the glass bulb volume is 10 times larger it will have a pressure of 0.95 mbar once sublimated.
4. Once ethanol is frozen out, close the valve, pump the mixing line, and fill the mixing line with 95 (10×9.5) mbar methanol.
5. Open the valve and the methanol will also freeze out.
6. Once methanol is frozen out, close the valve, pump the mixing line, and fill the mixing line with 104.5 (11×9.5) mbar CO. The pressure of CO is higher because CO does not freeze out at the temperature of LN_2 and thus $1/11^{\text{th}}$ of the CO will remain in the mixing line.

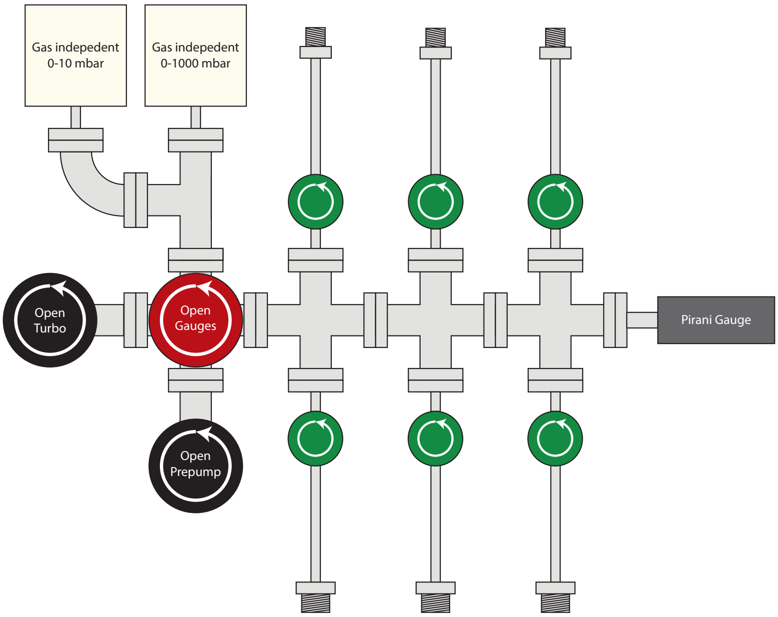

Figure 2.2: Schematic diagram of the mixing line used to prepare samples for the HV setup.

7. Open the valve and close the valve once the pressure between the glass bulb and mixing line is in equilibrium at 9.5 mbar.
8. Remove the LN_2 bath and wait for it to reach room temperature before use.

The relative accuracy of the mixture ratio is mostly dependent on the level of human reproducibility as the volume ratio is determined to be 6.9 ± 0.2 and the repeatability of the gauges is $\pm 0.01\%$ of the full range. For instance, when adding CO to the glass bulb when it is placed inside a LN_2 bath the pressure-to-volume ratio is not preserved. This is because the temperature of the CO gas drops once it collides with the cold surface and thus also the pressure. It is found that it is best to close the valve when the pressure gauge reads the desired pressure. This is prone to human error and was found to introduce errors up to 10% in the mixing ratios.

Typically, these gas samples are background deposited onto the ZnSe window at 15 K. This means that when molecules enter the chamber through the needle valve, they are pointed away from the substrate and interact first with the vacuum-chamber walls before adsorbing onto the window. The idea behind background deposition is that it mimics the adsorption of molecules in space onto dust grains with a random approach trajectory. Once the desired amount of molecules is deposited the deposition is stopped and infrared spectra are recorded. First a spectrum at 15 K is acquired after which the temperature of the ZnSe window is linearly increased with time. During the increase of the temperature, spectra are continuously acquired until all adsorbed species have sublimated. This allows to trace all changes in spectroscopic features as a function of temperature. This is done for acetaldehyde, dimethyl ether, and ethanol in Chapter 3 and for methyl formate in Chapter 4.

2.2 CryoPAD2

CryoPAD2 is an ultra-high-vacuum (UHV) system, which is used for the research presented in Chapter 6. It houses multiple diagnostic tools to investigate UV induced physical and chemical processes on analogue dust grains. The setup is build around a 9" spherical stainless steel chamber, which is fitted with 14 ports (one DN200CF, two DN100CF, three DN63CF, and eight DN40CF ports). The chamber is turbomolecular pumped by an Agilent TV 1001 navigator, which is connected at the bottom of the chamber and is backed by a Leybold Scrollvac 15 Plus. This turbo's pumping speed is specified at approximately 900 L s^{-1} for helium and hydrogen and results in a base pressure of low 10^{-10} mbar at room temperature and 4×10^{-11} mbar at cryogenic temperatures. The pressure is measured with a hot-cathode ionization gauge (DeMaco, Bayard-Alpert nude ion gauge) connected to a Granville-Phillips 350 vacuum gauge controller.

A closed-cycle helium refrigerator (ARS, DE202NB) is mounted vertically to the top port of the stainless chamber. This refrigerator allows for cooling of a gold-coated copper block that acts as an analogue substrate for a dust grain. The substrate is attached to the bottom of the second stage of the refrigerator where temperatures as low as 12 K can be reached. Typically, the substrate is aligned in the center of the chamber with other instruments. The refrigerator is connected to the chamber with both a two-stage differentially pumped rotary platform and Z-axis translator. The former allows for 360 degrees rotation of the substrate inside the chamber with 0.1 degree accuracy, and the latter allows the substrate to move up and down. This is particularly useful for characterizing the microwave-discharge hydrogen-flow lamp (MDHL), see Section 2.2.1.

The refrigerator has a certain cooling power and is either on or off, which means that in order to control the temperature of the substrate, heating power has to be applied. This is generally done through Joule heating, and allows us to control the temperature of the substrate from 12–300 K. A heating strip is attached to the second stage of the refrigerator, which can counteract some or all of the cooling power. The heating power is set by a PID controlled LakeShore 350 temperature controller that uses two Chromel–$\mathrm{AuFe}_{0.07\%}$ thermocouple (TC) temperature sensors as a feedback loop to probe the temperature of the substrate. One TC is mounted near the heating strip and one at the bottom of the substrate. The temperature is controlled on the TC near the heating strip and the experimental temperature is recorded with the TC at the bottom. The latter cannot be used for temperature control, as there is significant thermal mass between the heating strip and the bottom of the substrate. This would result in undesired oscillations in the temperature as the PID cannot compensate for this thermal lag. The TCs have an absolute accuracy of 2 K and a relative accuracy with respect to each other of 0.5 K. Molecular species can be deposited onto the substrate if the temperature of the substrate is below the desorption temperature of said species. The column densities, that is, molecules cm^{-2}, at which molecules are deposited can be controlled by the partial pressure at which the molecules are leaked into the chamber and the total exposure time. CryoPAD2 features a high-precision leak valve (Hositrad, VML14CFR16) followed by a glass-extruded capillary array. This deposition array allows for accurate control of the partial pressure and guarantees that the beam of molecules is close to collimated.

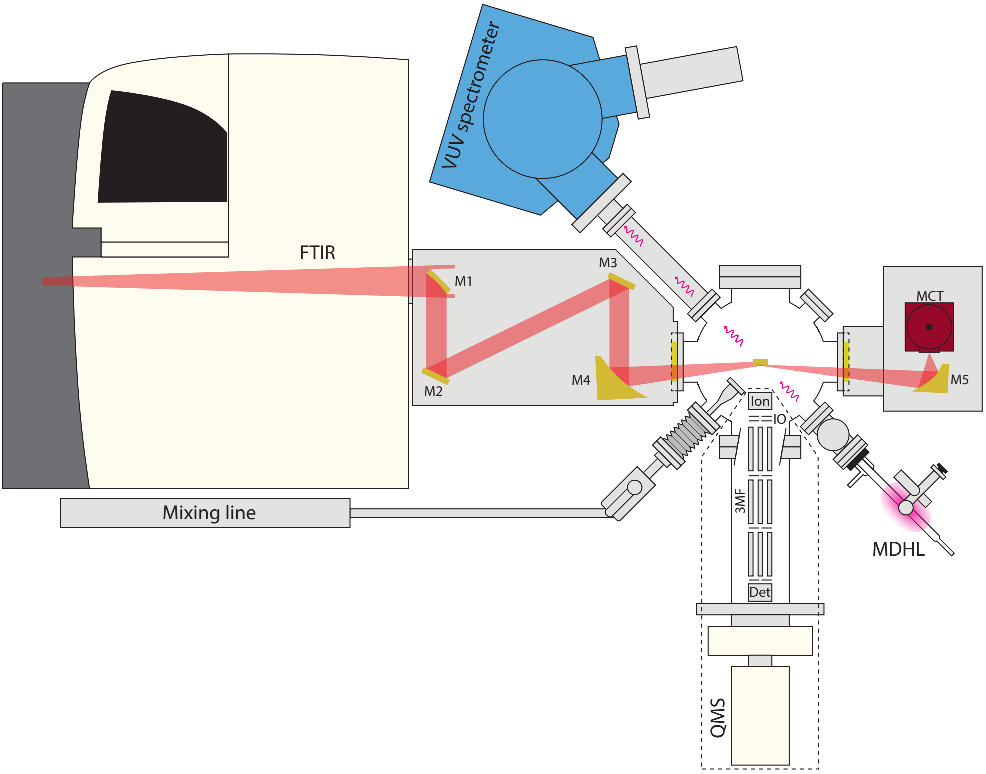

Figure 2.3: Top view schematic diagram of CryoPAD2 in the Laboratory for Astrophysics at Leiden Observatory.

Additionally, the deposition array is mounted on a linear UHV translator, which allows moving the deposition array from 50 mm to within 10 mm away from the substrate. The close proximity and collimated beam ensure that the majority of the molecules adsorb onto the subtrate, which reduces chamber contamination for subsequent measurements. The leak valve is directly connected to the mixing line of CryoPAD2. This mixing line is of similar design as that used for the HV setup, see Figure 2.2. However, here the sample is not stored in a glass bulb, but in the backbone of the mixing line, which allows direct deposition into the main chamber of CryoPAD2.

Once the desired species have been deposited, the experiment is usually continued by vacuum-UV irradiation of the sample. This radiation has the potential to break bonds of the parent deposited species, which can subsequently react with each other and form new species. Additionally, the excitation of species can result in the desorption of solid-state species into the gas phase. These processes are probed on CryoPAD2 through vibrational spectroscopy and mass spectrometry. The following sections describe the procedures and calibration used for the MDHL, reflection adsorption infrared spectroscopy (RAIRS), and quadrupole mass spectrometry (QMS).

2.2.1 Vacuum-UV irradiation

UV photons can get absorbed in the icy layer that cover the dust grains in the star- and planet-forming regions. In general, the absorption of a UV photon results in the increase of molecular complexity in these ices or the release into the gas phase through photodesorption. There are different sources of UV in these regions, that is, from the star itself, the external UV field from other stars, or through excitation of H or H_2. The UV emission from stars is broad band, while the excitation of hydrogen results in a rather discrete emission. The latter is simulated and used on CryoPAD2 with the use of a microwave-discharge hydrogen-flow lamp (MDHL).

Specifically, a T-type HDML is used through which H_2 (Linde, 99.999%) flows. The flow rate is set such that when the MDHL is pumped (Agilent TriScroll 300) the flow pressure equals 0.5 mbar, as measured by a Granville-Phillips Convectron gauge. The H_2 is initially excited with a high frequency generator (Electro-Technic Products BD-10A), and the plasma is sustained with a microwave cavity that is placed around the center of the lamp. The microwave cavity is air cooled and powered by a Sairem GMP 03 K/SM microwave generator. The spectral energy distribution (SED) of the MDHL is measured *in situ* on CryoPAD2 by a McPherson Model 234/302 VUV spectrometer. This spectrometer is mounted opposite of the MDHL and requires the gold-coated substrate to be raised with the Z-axis translator to clear the line of sight toward the spectrometer. The absolute UV flux is also measured *in situ* with a NIST calibrated SXUV-100 photodiode, which is mounted on two posts of PEEK at the bottom of the substrate. Full extension of the Z-axis translator puts the photodiode at the nominal height of the substrate, and allows for accurate determination of the vacuum-UV flux to which the samples are exposed.

Here only a brief description is given of the MDHL flux calibration, for more details see Ligterink et al. (2015). The photodiode has a relatively small band gap, which results in it being sensitive to photons with wavelengths < 1100 nm. Since the MDHL also produces photons in the visible range, these have to be excluded when measuring the photocurrent for flux calibration. The photocurrent is measured by a Keithley 485 picoammeter for both a standard open MDHL and a MDHL closed with a fused-silica window. The fused silica has a transmission wavelength of approximately > 200 nm, which means that the photocurrent measured with the closed MDHL is that attributed to visible photons. Subtracting this visible contribution from the total photocurrent of the open MDHL results in a photocurrent in the 115–200 nm range. However, fused silica is not fully transmissive and absorbs on general 10% of the visible photons. The vacuum-UV photocurrent, I_{VUV}, is then given by

$$I_{VUV} = I_{tot} - \frac{I_{vis}}{0.9}, \tag{2.1}$$

where I_{tot} is the total measured photocurrent with the open MDHL, I_{vis} the measured photocurrent with the closed MDHL, and 0.9 the correction for absorption of visible photons by the fused-silica window. However, this is not directly translatable into a photon flux as we lack the information on the contribution of each wavelength and the quantum efficiency of the photodiode. The percentage contribution of each wavelength is taken from Ligterink et al. (2015) and is used to scale the I_{VUV} to its respective wavelength bins. With the wavelength dependent quantum efficiency (η_q) supplied by the manufacturer, the photon flux for a given wavelength bin, $\Phi(\lambda)$, equals

$$\Phi(\lambda) = \frac{I_{VUV}(\lambda)}{e \cdot \eta_q(\lambda)}, \tag{2.2}$$

where e equals the charge of an electron in C. The photon flux as a function of wavelength is then integrated for the total vacuum-UV flux. In general, the flux is dependent on the conditions under which the lamp operates and is thus setup specific. Here the UV flux is $(2.5 \pm 0.3) \times 10^{14}$ photons s^{-1} cm^{-2}.

2.2.2 RAIRS

Species adsorbed on the gold-coated substrate are probed with an Agilent Cary 660 FTIR set up in reflection absorption infrared spectroscopy (RAIRS) mode. In this configuration, the infrared beam is coupled out of the FTIR, angled onto the gold-coated substrate under a grazing incidence, and reflected toward an external mercury cadmium telluride (MCT) detector. Atmosphere infrared absorption, that is absorption of infrared light by gas-phase H_2O and CO_2, is prevented by purging the infrared beam path outside the vacuum with dry air. The dry air is generated with a Pure Gas CO_2-PG80-2. The infrared beam from the FTIR is guided and focused by four gold-coated mirrors in the first purge box. The first mirror (M1, Thorlabs CM508-1000-M01) has a focal length of 1000 mm, which collimates the slightly diverging beam as it exits the FTIR, and M2 and M3 (Thorlabs PF20-03-M01) are two flat mirrors, which guide the collimated beam toward the off-axis parabolic mirror (M4, Thorlabs MPD399-M01). The off-axis parabolic mirror focuses the infrared beam under grazing incidence onto the gold-coated substrate. The reflected infrared beam is collected by a second off-axis parabolic mirror (M5), which focuses the infrared beam onto the MCT detector area in the second purge box. The infrared beam enters and leaves the vacuum chamber through two ZnSe windows. These windows are transparent in the infrared, but allow UHV conditions inside the main chamber.

An advantage of RAIRS is its increased sensitivity, which allows for detection of species with lower column densities over transmission spectroscopy. However, a downside of this is that the apparent transmission band strengths A' from literature are not applicable. When using RAIRS, a calibration is required to correct for the increased sensitivity in order to derive accurate column densities. Even this correction constant cannot be taken from literature, as it is dependent on the geometry of the infrared beam path and thus setup specific. In general, the column density of a species, $N_{species}$, measured through RAIRS is derived as follows

$$N_{species} = \ln(10) \cdot \frac{\int_{band} \log_{10}\left(\frac{I_0(\tilde{\nu})}{I(\tilde{\nu})}\right) d\tilde{\nu}}{R \cdot A'}, \tag{2.3}$$

where the prefactor ln(10) is the conversion from absorbance to optical depth, the numerator contains the integral of the absorption band of said species, and the denominator contains the RAIRS correction factor R and apparent transmission band strength A' for the integrated infrared band.

When the column density, $N_{species}$, is known, the RAIRS correction factor R can de derived by solving Eq. 2.3. A way to approximate the column density is through the change in binding energy of CO at different interfaces. The binding energy of

CO is lower when adsorbed on other CO molecules compared to adsorbed on the gold-coated substrate. This change in binding energy should become apparent when there is approximately one monolayer of CO on the substrate. Measuring the absorption band of CO at this turnover point in binding energy will allow solving for R when $N_{species}$ is set to 10^{15} molecules cm^{-2} in Eq. 2.3, where 10^{15} equals the column density of one layer of molecules on a surface.

Two methods have been used in the past on CryoPAD2 to find this turnover point in binding energy of CO. The first method is isothermal desorption of CO, here a multilayer of CO ice is heated to 27.5 K and is kept at this temperature. The CO starts to desorb at a slow rate, dependent on the temperature and binding energy, and once the majority of the "bulk" CO ice has desorbed the desorption rate slows down. This is because the average binding energy increases, as the remaining CO is adsorbed with a higher binding energy to the gold-coated substrate. By continuously acquiring infrared spectra during isothermal desorption the decrease in absorbance can be fitted by two slopes, one for the bulk CO and the other for CO on the substrate. The intercept of these slopes is where there is approximately one monolayer of CO on the surface (see e.g., Öberg et al. 2009c).

The second method that can be used is temperature programmed desorption (TPD) of different coverage of CO adsorbed on the substrate. Here the temperature at which CO desorbs is an indication of the binding energy of CO. By deposition of different column densities, one can derive from the TPD plot at what coverage there is approximately one monolayer on the surface and correlate this to the infrared absorption band measured for that coverage. A full description of this method is given in Chapter 2.3 of the PhD thesis of Ligterink (2017).

2.2.3 QMS

Molecules that desorb from the solid state into the gas phase, be it temperature induced or by photon processes, are recorded on CryoPAD2 by a Hiden HAL/3F PIC 1000 series quadrupole mass spectrometer (QMS). The QMS is mounted opposite of the RAIRS substrate surface at a distance of approximately 50 mm. This close proximity ensures the highest possible sensitivity of the QMS for desorbing species from the substrate. The basic principles of a QMS are described in Chapter 1.4.2, while here the calibration of the Hiden QMS for the mass sensitivity is discussed. A QMS is in general not equally sensitive to each mass over its measurable mass range. This is known as the mass sensitivity function (MSF) and once properly characterized it is used to correct the measured signals appropriately. This is important as without correction comparison with other experimental setups or databases, such as NIST[1], are very challenging.

The MSF is determined with a commercial mixture of noble gasses, that is, He, Ar, Kr, and Xe with a ratio of 0.884:0.0382:0.0390:0.0388, respectively. These noble gasses each have a different mass, and even different individual natural isotopes, which allows to probe the MSF in a range of different masses. The measured signals by the QMS, as a result of a constant leak rate of this noble gas mixture into the chamber, have to be corrected in order to compare them and derive the MSF.

---

[1] https://webbook.nist.gov/chemistry/

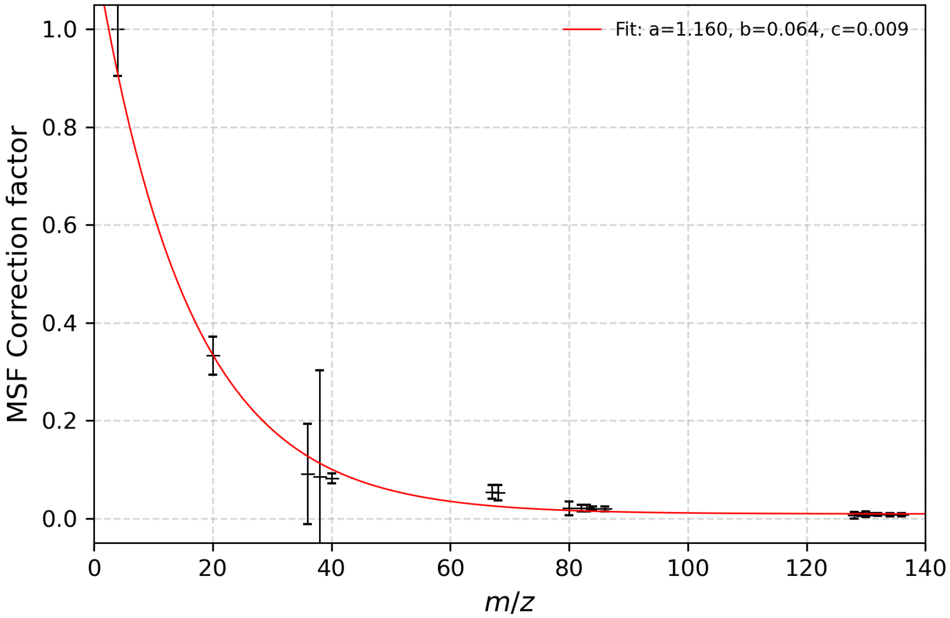

Figure 2.4: Mass sensitivity function derived with a noble gas mixture of He, Ar, Kr, and Xe. Black points shows the normalized signals after correction for the gas concentration, isotope abundance, and electron-impact ionization cross section and the red line is the fit to the data. The electron-impact ionization cross sections are take from Rejoub et al. (2002). The error bars on the data points are 2σ and derived from the standard deviation on the signals.

For example, the signal of ^{40}Ar is corrected as follows

$$S_{corr}(^{40}\mathrm{Ar}) = \frac{S_{QMS}(^{40}\mathrm{Ar})}{F(^{40}\mathrm{Ar}) \cdot I(^{40}\mathrm{Ar}) \cdot \sigma(^{40}\mathrm{Ar})}, \tag{2.4}$$

where S_{QMS} is the raw signal measure by the QMS, F the fraction of a species in a mixture, I the isotope ratio of that species in the fraction, and σ the electron-impact ionization cross section of that species. After this correction, each signal would be equal if the MSF was unity across the mass range. However, since this is not the case, the MSF for each mass can be approximated by fitting an exponential decay function, of the form $\mathrm{a} \cdot \exp(-\mathrm{b} \cdot \mathrm{x}) + \mathrm{c}$, to the normalized signals of the noble gasses as measured by the QMS after corrections. This fit and the normalized noble gas data after correction are shown in Figure 2.4. The fit of the MSF is used to find the correction factor for a given mass and is applied to all presented QMS data in this thesis.

2.3 ALMA

The Atacama Large Millimeter/submillimeter Array (ALMA) is a state-of-the-art radio interferometer, which consists of 54 12-meter and 12 7-meter diameter antennas. ALMA is the result of nearly 80 years of radio interferometry development. Radio interferometry dates back to the 1940s, where radio waves directly from a source and reflected on the surface of the sea interfered with each other and were observed with a single dish (sea-cliff interferometer). Great advances in the field were made with radio interferometers, such as the Owens Valley Radio Observatory (OVRO), Very Large Array (VLA), Combined Array for Research in Millimeter-wave Astronomy (CARMA), Westerbork Synthesis Radio Telescope (WSRT), Submillimeter Array (SMA), and Plateau de Bure (IRAM), that eventually led to development and construction of ALMA in the Atacama Desert of northern Chile. A full explanation of radio interferometry is beyond the scope of this thesis. However, a generalized basis is included to build a foundation for the methods used in Chapter 6.

In radio interferometry, aperture synthesis is used to combine the signals of all the antennas to produce a single image. This image is, however, not a true image of the sky, but a reconstruction that is retrieved from the phases and amplitudes of each of the antenna pairs. The use of aperture synthesis allows for high angular resolution observations with respect to the diameter of the antenna dish. This is because in interferometry, the Rayleigh criterion is not set by the individual antenna diameters, but the longest distance between antenna pairs. However, one cannot place two antennas at large distance and expect high image fidelity. In fact, this antenna pair is only sensitive to emission at those particular scales. In order to reach high fidelity the array of antennas needs to be configured in such a way that they cover a wide range of baseline lengths, where a baseline is the projected distance between an antenna pair.

Each antenna measures the phase and amplitude of the source they are pointing to. The signals of the different antennas are matched with each other by the correlator to create all the different baselines of the array configuration. In short, the correlators multiply and average the signals of all the antenna pairs and create a visibility for each baseline spatial frequency coordinate (u, v). Due to the rotation of the Earth, the baseline coordinates move across the uv-plane, which increases the uv-coverage. Figure 2.5 shows an example of the uv-coverage and visibilities as function of uv-distance of an ALMA execution block used in Chapter 5. One can directly work with these visibilities or Fourier transform them into the image plane. In this thesis, data reduction and analysis is performed in the image plane. Before looking into image restoration, it is however, important to first discuss calibration of the visibilities, the angular resolution, and the resulting maximum recoverable scale.

The amplitudes and phases measured for a source by each antenna pair are affected by several factors, such as amplitude changes and phase delays by the atmosphere. Without corrections for these errors, the observed brightness will be smeared out across the “sky” in the image plane. Through careful calibration of the data these errors can be removed or minimized. There are several types of calibration procedures and here we shortly discuss bandpass, phase, and flux calibration. These procedures are part of the ALMA pipeline and take place before the data is delivered to the principal investigator (PI). The initial step is to correct for variation in phase and amplitude as a function of frequency. This is achieved through bandpass calibration,

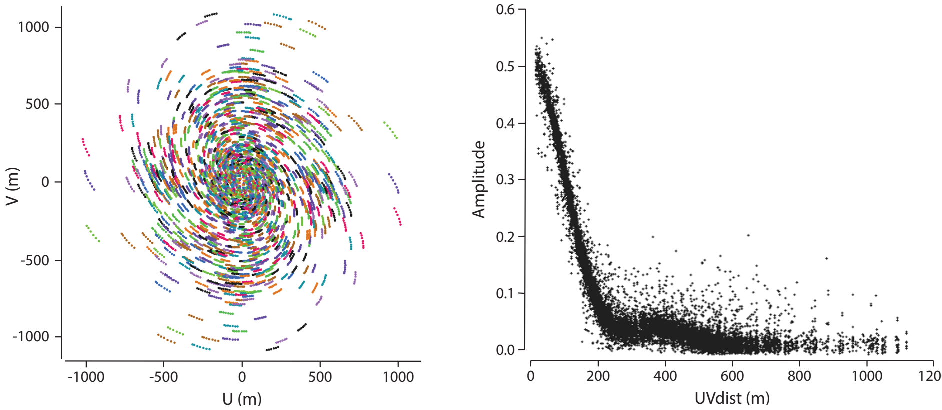

Figure 2.5: Left: Different baselines in the *uv*-plane from an observation of TW Hya with ALMA in Chapter 5. Right: Visibilities as a function of *uv*-distance for the baselines showed on the left.

which requires the observation of an additional source that is preferably unresolved and has a bright and flat featureless spectrum. After bandpass calibration, the phase and amplitude is calibrated as a function of time. In order to perform this phase calibration, the antenna array pointing is regularly switched between the science target and a nearby well defined source, often a quasar. Because these calibrator sources are well characterized, one can solve for the phase and amplitude of the science target as a function of time, assuming that between calibrator pointings the conditions are stable, such as the atmospheric conditions. The last step is flux calibration in which the absolute amplitude is scaled to a source of which the brightness is known. After the standard calibration is applied, provided that the signal-to-noise ratio is sufficiently high, minor residual errors can be removed with extra iterations of phase and amplitude calibration. This is known as self-calibration, and helps to increase the signal-to-noise ratio and the quality of the final image of the science target.

It is important to realize that an array of antennas in a specific configuration observes with a specific angular resolution and is only sensitive to those scales for which it is configured. For example, when observing a point source with an interferometer it does not appear as a point source in the image plane, as the interferometer has a finite resolution. The point source is observed with a certain point spread function (PSF), also known as the dirty beam, and the width of this beam determines how far apart two point sources on the sky can be spatially resolved from each other, that is, angular resolution. In star-forming regions the observed sources with ALMA are in general extended and resolved. This allows us to look at for instance the gas and dust of a protoplanetary disk as a function of radius from the star. However, one should be careful with high angular resolution observations of extended sources. Interferometers have a finite amount of antennas available to create baselines, and in order to create high angular resolution observations, many of these antennas are placed at long distances from each other. As mentioned earlier, a baseline is only susceptible to a specific scale and by removing short baselines in favor of long baselines, sensitivity to the larger angular scales on the sky is lost. This results in a so-called maximum recoverable scale (MRS) of a particular array configuration. In general, an array configuration with finite antennas can have an increased angular resolution, but at the cost of a loss of information on the true sky distribution at scales larger than the MRS.

The shape of the PSF is determined by the array configuration and its resulting *uv*-coverage. However, it is also dependent on how each baseline is weighted. There are several ways in which the baselines can be weighted. The possible weighting schemes are natural, uniform, Briggs, or tapering. In natural weighting, each baseline is weighted equally and results in the highest possible signal-to-noise ratio at modest angular resolution. The uniform weighting scheme decreases the weighting of a baseline depending on the number of baselines in a certain *uv*-grid cell (for fast Fourier transform the *uv*-plane is divided into a 2D grid), and results in the highest possible angular resolution of the array configuration at the cost of poorer signal-to-noise ratio. A balance between uniform and natural weighting can be found with Briggs weighting, where the robust parameter determines how weighting is applied. The robust parameter ranges from -2 to 2, where -2 is close to uniform and 2 is close to natural weighting (Briggs 1995). In general, for ALMA the advised weighting scheme is Briggs with a robust parameter of 0.5, as this gives the best balance between angular resolution and signal-to-noise ratios for the designed array configurations. Tapering is a weighting scheme in which the visibilities are scaled in the *uv*-plane with an elliptical Gaussian, which reduces the weight as the baseline length increases with a Gaussian profile. This is particularly useful for improvement of the synthesized beam shape, but comes at the cost of angular resolution.

Once the desired weighting scheme is chosen, image restoration algorithms can be used to improve the image quality. The image created from the initial Fourier transform is called a dirty image because the true on sky distribution is observed with a PSF that contains sidelobes. These sidelobes smear out the emission and create artifacts that do not represent the on sky distribution. These sidelobes exist because the *uv*-plane is not complete, it is only measured at discrete *uv*-coordinates. The gaps in the *uv*-plane can contain any value and result in an infinite amount of solutions for the Fourier transform into the image plane. A solution to this is setting all the unknown values to zero, the so-called principle solution. However, a result of this is that the PSF can have very significant sidelobes that distort the dirty image.

A way to improve this is through a restoration algorithm, which can guess more reasonable values than zero for these unknown values. A commonly used algorithm is the CLEAN algorithm developed by Högbom (1974). In this algorithm, a model of point sources is created, which is then convolved with a synthesized beam that represents the PSF without sidelobes. This model is created by scaling the PSF to the brightest position in the dirty image and subtracting a portion (gain factor < 1) of the PSF from the dirty image. The subtracted flux is stored and represented as a point source in the model. This is an iterative process that is repeated until a user specified threshold level is reached. What remains below the threshold level is called the residuals and in general this should contain noise or emission not distinguishable from noise. A good rule of thumb is to set the threshold to three times the noise level. After the threshold is reached the model is convolved with a synthesized beam representing the PSF and the residuals are added to form a CLEANed image. An example of a dirty image and CLEANed image is shown in Figure 2.6.

In this thesis, the Common Astronomy Software Applications (`CASA`) 5.6.1 is used to reconstruct the images with the `TCLEAN` task (McMullin et al. 2007). However, instead

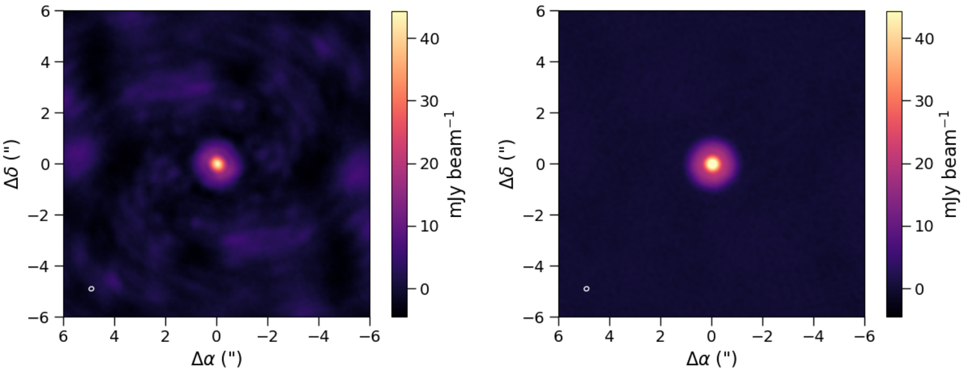

Figure 2.6: Dirty (left) and CLEANed (right) image of the 351 GHz continuum of TW Hya observed with the band 7 receivers. The angular resolution of these observations is shown shown in the bottom left with a white ellipse.

of the default Högbom deconvolver the multiscale deconvolver is used, which was developed by Cornwell (2008). This particular deconvolver creates a model consisting of Gaussian objects of a given set of scales rather than only points sources. It is found that this type of deconvolver is more accurate at guessing/predicting the unsampled regions in the *uv*-plane for extended sources compared to the Högbom deconvolver. One should, however, always keep in mind that the restored images are only one of the infinite solutions possible through Fourier transform of a discrete sampled *uv*-plane. The user and algorithm try to infer the best possible values for unsampled *uv*-coordinates, but they can under- or over-predict flux at scales that the array inherently was not sensitive to.

2.3.1 Keplerian masking of rotating disks

Figure 2.6 shows the spatially resolved continuum emission of the dust at approximately 351 Ghz in the disk of TW Hya. Besides the unprecedented spatial resolution, ALMA also has high spectral resolution. Because of this spectral resolution, ALMA is able to spectrally resolve emission of gas-phase molecules. This is particularly useful as it allows to resolve the Keplerian rotating gas around a young star into different channels. An example of Keplerian rotating gas can be seen in Figure 5.1 of Chapter 5. The observed H_2CO gas moves at different velocities with respect to us due to the inclination of the disk around TW Hya. This Doppler shift in velocity can be predicted for each pixel when the stellar mass is known and used to mask the pixels in channels where Keplerian rotating gas is expected. The shaded areas in Figure 5.1 show where Keplerian rotating gas is expected.

It is common to integrate over velocity spaces to create a single image that displays the emission of a gas. The velocity integrated emission map, also known as moment-zero map, is basically the summation of the different channels that contain emission of Keplerian rotating gas. The signal-to-noise ratio of these maps can be improved by exploiting the knowledge of Keplerian rotation and exclude the regions that only contain noise and no Keplerian emission. This method is used in Chapter 5, but for example also in the studies by Walsh et al. (2016) and Salinas et al. (2017).